Phonon Topology and Winding of Spectral Weight in Graphite

N. D. Andriushin,[1] A. S. Sukhanov,[1] A. N. Korshunov, M. S. Pavlovskii,[2] M. C. Rahn,[1] and S. E. Nikitin[3,4,*]
[1]Institut für Festkörper- und Materialphysik, Technische Universität Dresden, D-01069 Dresden, Germany
[2]Kirensky Institute of Physics, Siberian Branch, Russian Academy of Sciences, Krasnoyarsk 660036, Russian Federation
[3]Quantum Criticality and Dynamics Group, Paul Scherrer Institut, CH-5232 Villigen-PSI, Switzerland
[4]Laboratory for Neutron Scattering and Imaging, Paul Scherrer Institut, CH-5232 Villigen-PSI, Switzerland

(Received 17 March 2023; accepted 19 October 2023; published 14 December 2023)

The topology of electronic and phonon band structures of graphene is well studied and known to exhibit a Dirac cone at the K point of the Brillouin zone. Here, we applied inelastic x-ray scattering (IXS) along with *ab initio* calculations to investigate phonon topology in graphite, the 3D analog of graphene. We identified a pair of modes that form a very weakly gapped linear anticrossing at the K point that can be essentially viewed as a Dirac cone approximant. The IXS intensity in the vicinity of the quasi-Dirac point reveals a harmonic modulation of the phonon spectral weight above and below the Dirac energy, which was previously proposed as an experimental fingerprint of the nontrivial topology. We illustrate how the topological winding of IXS intensity can be understood in terms of atomic displacements and highlight that the intensity winding is not in fact sensitive in telling quasi- and true Dirac points apart.

DOI: 10.1103/PhysRevLett.131.246601

Introduction.—The mathematical concept of topology has become a key concept of modern condensed matter physics [1,2]. Topology allows one to classify continuous manifolds and thus provides a new organizing principle for the electronic band structure of solids [3,4]. The textbook example is the honeycomb structure of graphene, whose triangular Bravais lattice precludes a hybridization of the orthogonal electronic states originating from its two-atomic basis. Electrons in the vicinity of the resulting linear band crossing behave as massless quasiparticles described by the Dirac equation and are responsible for many unconventional transport effects.

Notably, the concept of topology does not depend on details of quantum statistics and is just as applicable to bosonic quasiparticles such as phonons [5] or magnons [6]. The theoretical study of phonon topology has recently attracted special interest. Significant advances include the prediction of a surface arc state in hexagonal WC (tungsten carbide) type materials [7], quadratic nodal lines and hybrid nodal rings in AgZr [8], and topological gimbal phonons in T-carbon [9]. Experimentally, the topology of lattice fluctuations is also being actively studied in artificial mesoscopic structures with linear dimensions of the order of millimeters, resulting in resonance frequencies in the kilohertz range. These developments have in fact coined a new research field—topological acoustics [10–12]. However, in conventional crystals with interatomic distances of several angstrom and vibration frequencies of $\approx$10 THz, the unambiguous identification of topological phonon crossings remains a challenge, and only few reports have been published so far [13–15]. A common approach in this field is to characterize the dispersion in the vicinity of crossing points and compare this data with *ab initio* calculations. Nontrivial topological properties can then be inferred from the analysis of the calculated phonon dispersions. Crucially, this does not provide an immediate experimental probe of topology, rather than a verification of the density functional theory.

Recently, Jin *et al.* [15] proposed an experimental method to probe topological character of a phonon crossing by measuring the spectral weight in its vicinity. The same approach is already widely used in application to the magnon band structure [16–19]. It reads that on closed momentum-space contours around the crossing point, the intensity of phonon excitations is modulated, with a number of minima and maxima related to the Berry phase of the point. This phenomenon results from the modulation of phonon eigenvectors around the crossing point. It was therefore proposed as a direct experimental probe of the phonon topology.

In the present Letter, we apply this method to study low-energy phonons in the vicinity of the K point in graphite using inelastic x-ray scattering (IXS) and density-functional theory (DFT) calculations [see Sec. S1 of Supplemental Material (SM) [20] for method details] and demonstrate the limitations of such approach, which were not previously pointed out. Graphite consists of graphene layers stacked with a relative shift of $[2/3, 1/3, 0]$ along the ab plane [known as the AB stacking, Fig. 1(a)]. Although its phonon dispersions were previously mapped in detail throughout the entire Brillouin zone (BZ) [31,32], the distribution of the spectral weight, which carries the crucial information on the eigenvector modulation, has not been addressed. We identified both theoretically and

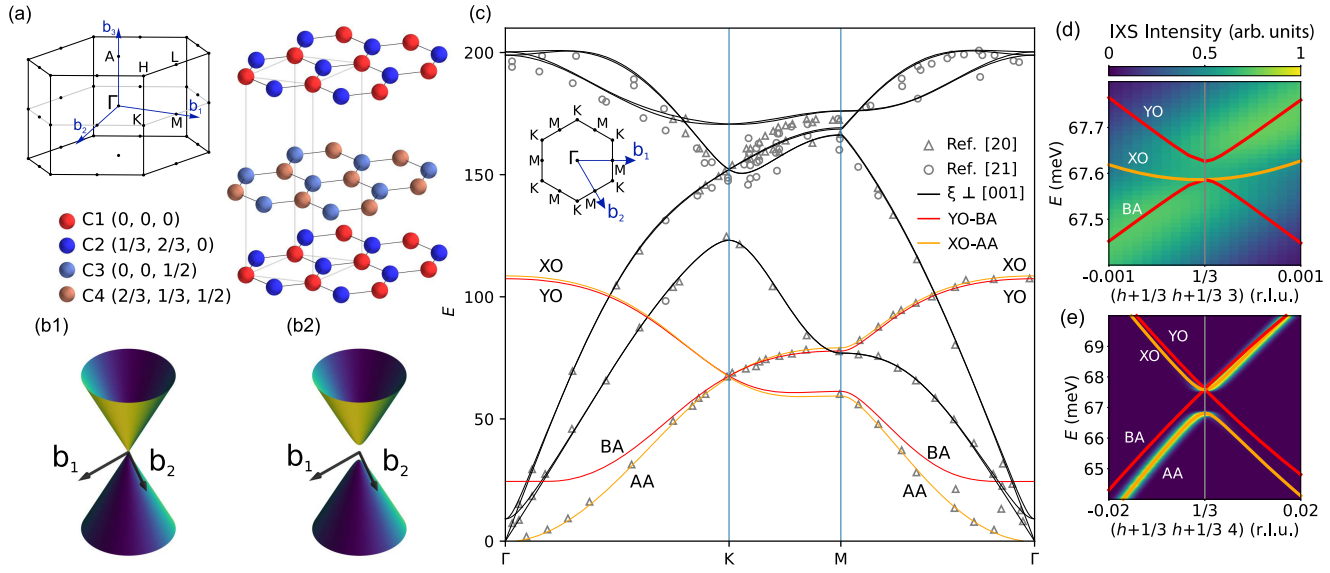

FIG. 1. Crystal structure and phonon excitations in graphite. (a) The crystal structure, formed from an AB stacking of honeycomb layers, and the first Brillouin zone. (b1),(b2) Schematic representation of the phonon dispersion around the K point, showing the gapless Dirac cone in graphene (b1), which gaps out due to interlayer coupling in graphite (b2). (c) Comparison of our DFT calculation (solid lines) of the phonon dispersion in graphite with previous IXS measurements [31,32]. The first BZ of graphite within the $(hk0)$ plane is shown in the inset. (d),(e) Detailed view of the YO–BA (red line) and XO-AA (orange line) modes in the vicinity of K along $(hh3)$ and $(hh4)$ paths of reciprocal space (see details of reciprocal-space trajectories in Sec. S2 of SM [20]). The color map indicates the simulated IXS intensity.

experimentally that there exists a pair of low-energy modes that form a weakly gapped pseudo-Dirac cone at the K point. Our IXS data demonstrate the antiphase distribution of the phonon spectral weight above and below the pseudo-Dirac point, in perfect agreement with the theoretical predictions applied for a true Dirac point. Our DFT calculations illustrate that the microscopic origin of this winding pattern lies in the relative phase shift of out-of-plane oscillations of two atoms within the honeycomb layers. The latter remains intact upon opening of a barely noticeable gap at the Dirac point caused by small but finite perturbative interlayer interaction.

Overview of the phonon dispersion.—We start the presentation of our results with a brief overview of the phonon dispersion of graphite, shown in Fig. 1(c) [31–34]. Our DFT calculations of the dispersion fully corroborate previous measurements and calculations [35,36]. Based on this excellent agreement, we can use this model to simulate the distribution of the phonon spectral weight and relate it to the structural fluctuation patterns in the vicinity of the K point.

We can broadly categorize all modes in Fig. 1(c) into two groups: low-energy c-polarized modes (black lines) and high-energy modes with $\perp$ [001] (orange and red lines). Visual inspection of Fig. 1(c) suggests that the dispersion has several crossings at the K point at $E = 67$, 152, and 170 meV. However, the modes close to K points at energies $\approx$152 and 170 meV have shallow dispersion and remain linear only within a narrow energy range of $\lesssim$1.5 meV, which means they can be classified as not "clean" crossings according to criteria defined in Ref. [37]. Therefore, we focus on the low-energy part of the spectrum. It contains four modes: the acoustic (AA) and the low-energy pseudo-acoustic (BA) modes, and two almost degenerate downward-dispersing optical branches, (YO) and (XO), at 65–110 meV. The AA and BA modes are related to in-phase and antiphase fluctuations of carbon layers along the c axis, and their splitting is determined by the strength of the interlayer coupling. Furthermore, the structure factor $F^{(s)}(\mathbf{Q})$ has a profound impact on the observable intensity, which allows us to separate the modes: (i) both modes have finite intensities only at nonzero l (l is the reciprocal space coordinate); (ii) due to the structure factor modulation, AA and BA intensities are harmonically modulated along the l direction and acquire maximal intensity at even and odd l, respectively.

The acoustic and optical c-polarized phonon modes in graphene are known to form a Dirac cone centred at the K point as shown in Fig. 1(b1) [36]. However, in graphite, a finite interlayer coupling breaks the inversion symmetry between the carbon atoms within a honeycomb layer and gaps out the otherwise degenerate states at the K point, causing the typical anticrossing behavior [Fig. 1(b2)] [35]. To visualize this effect, in Fig. 1(e) we show the calculated IXS intensity for the slice along the $(hh4)$ direction that maximizes intensity of XO and AA modes. Here, a gap of $\sim$0.8 meV is clearly visible at the K point. The YO and BA modes are best visible at odd l and almost degenerate

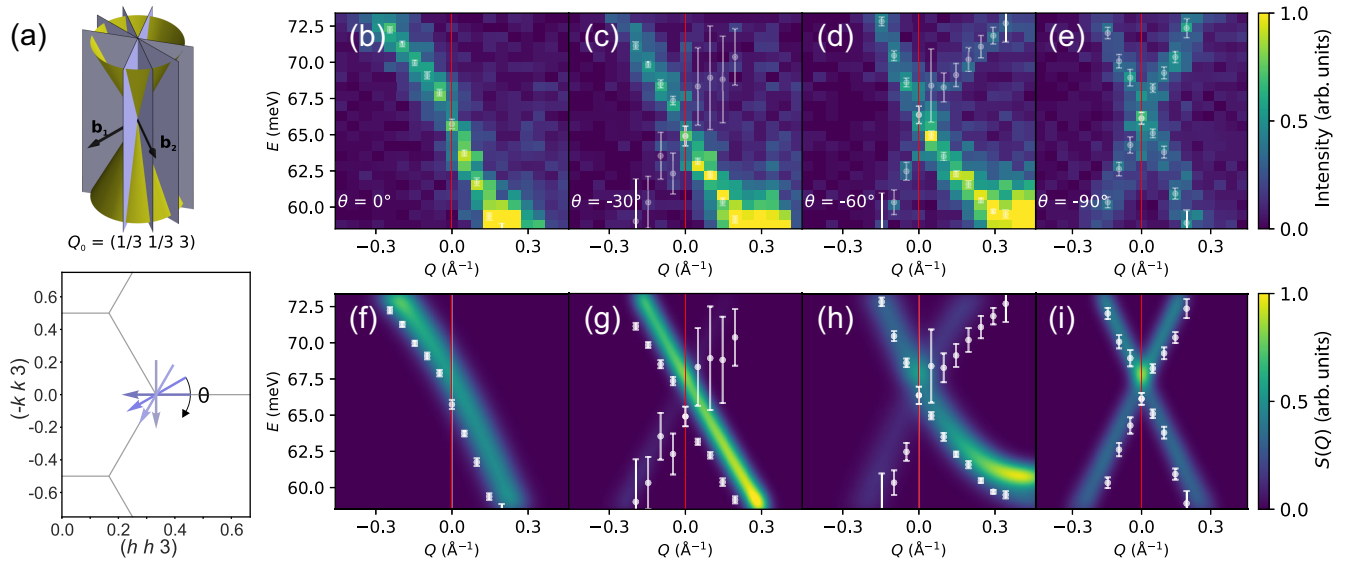

FIG. 2. Phonon dispersion in the vicinity of the K point at $\mathbf{Q} = (1/31/33)$. (a) Schematic of the slices through 4D energy-momentum reciprocal space. (b)–(e) IXS data along selected radial directions centered at the K point. Note that additional intensity at $E < 61$ meV in (b) and (c) is due to contribution from the second crystal domain in the sample. (f)–(i) Corresponding simulated IXS spectra. White symbols denote the fitted peak positions with 95% confidence interval [20].

at the K point with an extremely small gap of ∼50 μeV [Fig. 1(d)]. We should stress that these modes do not form a true topologically protected crossing as the mode repulsion is induced by a weak interlayer interaction. However, the splitting of the YO–BA mode pair is in essence irrelevant for the given slope of the linear dispersion, i.e., everywhere except for the vanishingly narrow momenta range of $\kappa_0 \approx \pm 10^{-3}$ r.l.u., as we discuss in detail in Sec. S4 of SM [20]. Below we demonstrate that the distribution of the phonon spectral weight in the vicinity of the K point but at any momenta greater than κ_0 follows the characteristic intensity winding behavior, which was deemed to only accompany a true Dirac point. We then focus on the K point of $\mathbf{Q} = (1/3, 1/3, 3)$, where the structure factor maximizes the scattering intensity of the weakly repulsed YO and BA modes.

IXS spectra.—Figure 2 illustrates the variation of the IXS spectra around $\mathbf{Q} = (1/3, 1/3, 3)$. The orientation of four energy-momentum slices with respect to the phonon Dirac cone is visualized in Fig. 2(a). Figure 2(b) shows the longitudinal slice along the $(hh3)$ direction. It features a single, linearly dispersing phonon mode that crosses the K point at Dirac energy $E_{\mathrm{Dirac}} = 65.6(2)$ meV, slightly below the calculated value of 67 meV. Figures 2(c) and 2(d) show spectra along two radial paths, rotated by 30° and 60° to the $(hh3)$ direction, respectively. The signal in Fig. 2(c) looks rather similar to the $(hh3)$ path, with only a faint trace of the second mode, which becomes clearly visible in the data in Fig. 2(d). Figure 2(e) shows the radial slice along the $(1/3 - k, 1/3 + k, 3)$ direction, i.e., orthogonal to $(hh3)$. It exhibits an X-shaped crossing at the K point. The two crossing modes have similar IXS intensity over the whole energy range, in agreement with the simulated spectrum, Fig. 2(i). Taken together, our data indicate good agreement with the simulated spectra and show that YO and BA modes touch at the K point within our instrumental resolution, and exhibit the linear dispersion within $\approx \pm 0.1$ Å^{-1}, followed by some extended quasilinear regime up to $\approx \pm 0.3$ Å^{-1} (see Ref. [20] for a strict criteria of nonlinearity). The spectral weight is gradually redistributed over both modes under rotation around the K point. All DFT results are in good agreement with these observations. We further comment that the calculated gap at K point for YO–BA crossing is only ∼50 μeV, which is well below the experimental resolution and therefore cannot be resolved in our data.

Having discussed the dispersion around the K point, we turn to the quantitative analysis by plotting the IXS intensity on radial constant-energy paths through the K point. Figures 3(a) and 3(b) show a series of these slices at 62.2 and 70.4 meV, below and above the Dirac energy $E_{\mathrm{Dirac}} \pm 4$ meV. Figure 3(c) illustrates the trajectories of these scans and our definition of an angle θ with respect to the $(hh3)$ direction. Each slice was fitted using two Lorentzians to quantify the spectral weight of each phonon mode. In Fig. 3(d), we summarize these peak areas as a function of the angle θ. This reveals harmonic oscillations described by

$$I(\theta) = a_0[1 \pm \cos(\theta)], \tag{1}$$

for energies above and below the Dirac energy, respectively, with a_0 as a constant prefactor. This result is perfectly consistent with our DFT simulations and the

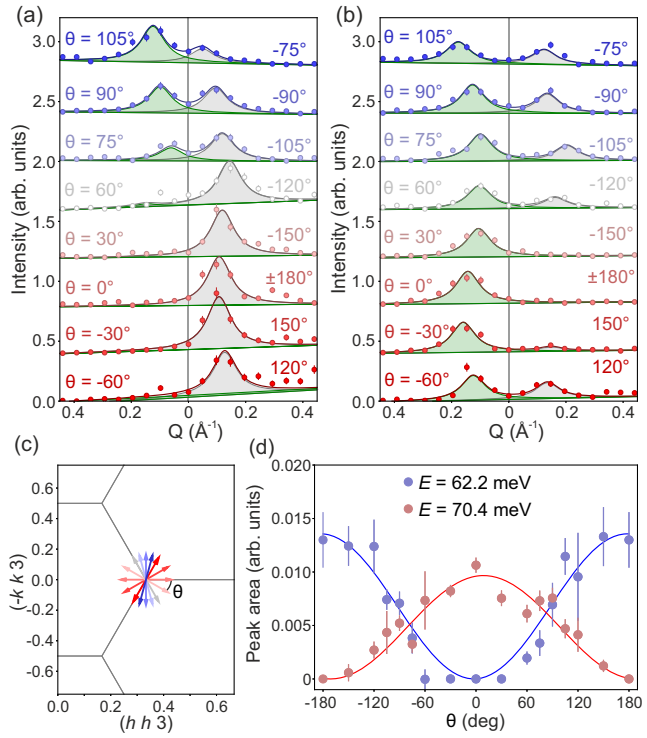

FIG. 3. Modulation of the phonon spectral weight in graphite. (a),(b) Radial momentum profiles of IXS intensity through the K point in the $(hk3)$ plane at $E = 62.2$ (a) and 70.4 meV (b). Solid lines represent a complete fit to the data that includes phonon contributions (Lorentzian peaks) and a linear background. Green and gray shaded areas show the phonon peaks measured on the opposite trajectories off the K point. The data are offset by $+0.4$ units for visual clarity. (c) Trajectory of the momentum profiles shown in (a) and (b), and the definition of the angle θ. (d) θ dependence of the peak area extracted from the IXS measurements. Solid lines are fits with Eq. (1).

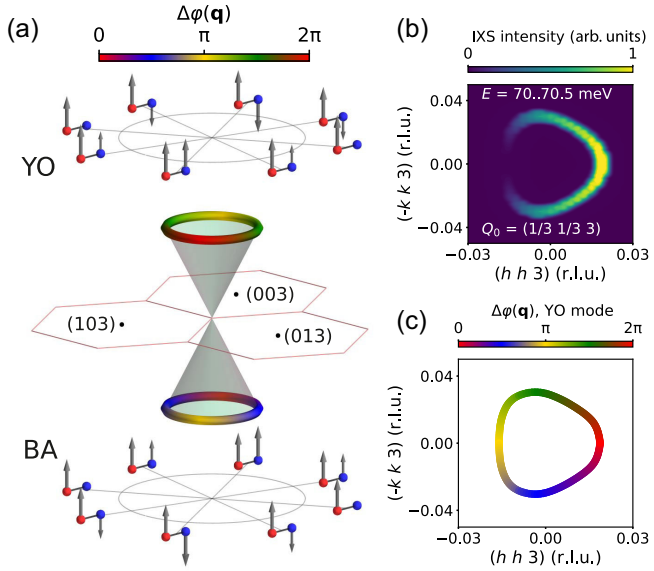

FIG. 4. Microscopic origin of the intensity winding. (a) Schematic representation of the pseudo-Dirac cone. Color plots at the cone bases represent phase difference of two atomic displacements, $\Delta\varphi(\mathbf{Q})$. Two sketches above and below the pseudo-Dirac cone demonstrate the calculated atomic displacements of two atoms within the honeycomb layer, ξ_1 and ξ_2, at several equidistant $\mathbf{Q}$ points. (b) IXS intensity distribution within the $(hk3)$ plane calculated at $E = [70, 70.5]$ meV, above the pseudo-Dirac point. (c) Phase difference of two atomic displacements $\Delta\varphi(\mathbf{Q})$ calculated for the same energy.

theoretically predicted modulation for a Dirac point [15]. Notably, a similar modulation of spectral weight was observed in several magnonic honeycomb ferromagnets including $CoTiO_3$ [17,38], elemental Gd [18], and $CrBr_3$ [19].

Microscopic origin of the intensity modulation.—Our IXS data shown in Fig. 3(d) demonstrate a smooth modulation of the phonon spectral weight. To provide an intuitive picture of how this winding relates to atomic displacements, we further examine the results of our DFT simulations. The dispersions of the YO and BA modes were calculated on a closed contour around the K point (diameter $|\Delta\mathbf{Q}| = 0.02$ Å^{-1}), just above and below the pseudo-crossing. Within the considered $\mathbf{Q}$ range, the dispersion of both modes remains almost flat. Moreover, because the modes are polarized along the c axis [Fig. 1(c)], the eigenvector of each phonon mode close to the pseudo-Dirac point (the same, in principle, applicable to a true Dirac point as well) can be characterized by four complex numbers, which represent the displacements of four atoms (two atoms per layer) within the unit cell.

However, because we are interested in the in-plane dispersion, the problem can be simplified. Given that at every $\mathbf{Q}$ point of interest the two layers exhibit antiphase vibrations, these modes can be described using only the displacements of the two atoms in a honeycomb layer, $\xi_1^z(\mathbf{q})$ and $\xi_2^z(\mathbf{q})$. An analysis of the eigenvectors shows that $|\xi_1^z(\mathbf{q})| \approx |\xi_2^z(\mathbf{q})| = \xi_0^z$ and, thus, the phase difference between the eigenvectors of the two atoms, $\Delta\varphi(\mathbf{q}) = \arg[\xi_1^z(\mathbf{q})] - \arg[\xi_2^z(\mathbf{q})]$, is the primary parameter that controls the distribution of the spectral weight around the K point. To demonstrate this, in Fig. 4(a) we plot the calculated $\Delta\varphi(\theta)$ for energies above and below the Dirac energy. This shows a continuous rotation around the K point, with a relative shift of π for energies above and below the Dirac point. To visualize how the phase difference relates to atomic motion, in Fig. 4(a) we present evolution of the atomic displacements, $\xi_1^z(\mathbf{q})$ and $\xi_2^z(\mathbf{q})$, for several $\mathbf{Q}$ points on a circle around K for both energies.

Now we show analytically how the phase difference causes the intensity redistribution. We substitute the eigenvectors in a form $\xi_i^z(\mathbf{q}) = |\xi_0^z| e^{i\varphi_i(\mathbf{q})}$ in the standard equation for the IXS intensity [20] and find that $|F^s(\mathbf{q})|^2 \propto 1 + \cos[\Delta\varphi(\mathbf{q})]$. Since $\Delta\varphi \propto \theta$ [see Fig. 4(c)], the IXS intensity exhibits the gradual harmonic modulation

[Fig. 4(b)]. That provides an intuitive microscopic explanation for the observed cosine modulation of the intensity around the Dirac point in graphite, in accordance with Eq. (1) (see Sec. S3 of SM [20] for the detailed derivation).

Discussion and conclusion.—Topological bosonic quasiparticles have been actively studied in condensed matter physics over the past years [6,36–39]. The majority of experimental studies were aimed at determining the *dispersion* in the vicinity of a crossing point of interest, while the intensity distribution is rarely inspected in detail [13,14,40,41]. However, one striking feature of topological crossings is that some physical quantity should exhibit a winding around it. Usually, the winding is associated with a pseudo-spin of a low-energy Hamiltonian that describes the dynamics of a model close to the crossing point [42]. Coming back from pseudo-spin to phonon or magnon terminology, this corresponds to a rotation (in a broad sense) of the eigenvector on a close path around the crossing point. This will be reflected in a physical observable like the spectral weight in a scattering experiment, thus providing a direct measure of topological charge [15].

Here, we have applied this idea to address the low-energy linear phonon crossings in graphite, one of the simplest honeycomb systems. Our DFT calculations indicate that the interlayer coupling is a relevant perturbation that breaks the symmetry between the two carbon atoms within a honeycomb layer and hybridizes the otherwise crossing YO–BA modes at the K point. The gap is controlled by strength of interlayer coupling and amounts to only $\sim$50 μeV. Because the interlayer coupling in graphite is induced by weak Van der Waals forces, it can be noticeably enhanced by hydrostatic pressure. This way one can effectively push the system toward 3D regime and increase the gap at the K point. In this case, a large gap breaks the winding of the spectral weight and pseudo-Dirac states no longer exist [20].

However, the resulting avoided crossing of the YO–BA modes plays a role only in the momenta scale as small as $\sim 5 \times 10^{-4}$ Å^{-1} away from the K point in the absence of external pressure. Outside this narrow region, the modes in essence behave indistinguishably from modes forming a true Dirac point, hence referred to as the pseudo-Dirac cone. Because the gap is too small to be resolved in an experiment, our IXS data show that the YO and BA modes exhibit a linear crossing at the K point, and also provide a clear evidence for *intensity winding* with opposite phases above and below E_{Dirac}. This result is in perfect agreement with the theoretical expectations for the $\pm\pi$ Berry phase on a contour surrounding a Dirac point. By analyzing the displacement vectors, we show that the relevant physical quantity which winds and produces this peculiar intensity distribution is $\Delta\varphi$, the phase difference between the oscillation of the two atoms in the honeycomb plane.

Therefore, the approach of identifying the intensity winding cannot be solely applied when the topological properties of the band structure are addressed. Our results indicate that the experimental observation of intensity modulation proposed in Ref. [15] for the phonon bands and already widely used in application to the magnon bands [17–19] can only serve as a fingerprint of the winding of quasiparticle eigenvector rather than prove existence of a topologically protected crossing, unless the measurements are taken on a scale of the smallest gap in the system, that is often not possible due to resolution broadening, especially in low-dimensional systems such as graphite with strong hierarchy of couplings. We have thus identified winding of the phonon eigenvectors due to proximity to a pseudo-Dirac point and show how IXS can be applied to study topological lattice excitations in condensed matter systems.

We thank R. Coldea for stimulating discussions. A. Bosak participated in the discussion and preparation of the experiment. We acknowledge financial support from the Swiss National Science Foundation, from the European Research Council under the grant Hyper Quantum Criticality (HyperQC), the German Research Foundation (DFG) through the Collaborative Research Center SFB 1143 (Project No. 247310070), and from the European Union Horizon 2020 research and innovation program under Marie Skłodowska-Curie Grant No. 884104. We acknowledge the European Synchrotron Radiation Facility (ESRF) for provision of synchrotron radiation facilities.

*Corresponding author: stanislav.nikitin@psi.ch

[1] S. M. Bhattacharjee, M. Mj, and A. Bandyopadhyay, *Topology and Condensed Matter Physics* (Springer, New York, 2017), Vol. 19.
[2] J. Wang and S.-C. Zhang, Topological states of condensed matter, Nat. Mater. **16**, 1062 (2017).
[3] A. Bansil, H. Lin, and T. Das, Colloquium: Topological band theory, Rev. Mod. Phys. **88**, 021004 (2016).
[4] P. Narang, C. A. C. Garcia, and C. Felser, The topology of electronic band structures, Nat. Mater. **20**, 293 (2021).
[5] Y. Liu, X. Chen, and Y. Xu, Topological phononics: From fundamental models to real materials, Adv. Funct. Mater. **30**, 1904784 (2020).
[6] P. A. McClarty, Topological magnons: A review, Annu. Rev. Condens. Matter Phys. **13**, 171 (2022).
[7] Q. Xie, J. Li, S. Ullah, R. Li, L. Wang, D. Li, Y. Li, S. Yunoki, and X.-Q. Chen, Phononic Weyl points and one-way topologically protected nontrivial phononic surface arc states in noncentrosymmetric WC-type materials, Phys. Rev. B **99**, 174306 (2019).
[8] F. Zhou, Z. Zhang, H. Chen, M. Kuang, T. Yang, and X. Wang, Hybrid-type nodal ring phonons and coexistence of higher-order quadratic nodal line phonons in an AgZr alloy, Phys. Rev. B **104**, 174108 (2021).
[9] J.-Y. You, X.-L. Sheng, and G. Su, Topological gimbal phonons in T-carbon, Phys. Rev. B **103**, 165143 (2021).

[10] Z. Yang, F. Gao, X. Shi, X. Lin, Z. Gao, Y. Chong, and B. Zhang, Topological acoustics, Phys. Rev. Lett. **114**, 114301 (2015).

[11] X. Zhang, M. Xiao, Y. Cheng, M.-H. Lu, and J. Christensen, Topological sound, Commun. Phys. **1**, 97 (2018).

[12] H. Xue, Y. Yang, and B. Zhang, Topological acoustics, Nat. Rev. Mater. **7**, 974 (2022).

[13] H. Miao, T. T. Zhang, L. Wang, D. Meyers, A. H. Said, Y. L. Wang, Y. G. Shi, H. M. Weng, Z. Fang, and M. P. M. Dean, Observation of double Weyl phonons in parity-breaking FeSi, Phys. Rev. Lett. **121**, 035302 (2018).

[14] T. Nguyen, F. Han, N. Andrejevic, R. Pablo-Pedro, A. Apte, Y. Tsurimaki, Z. Ding, K. Zhang, A. Alatas, E. E. Alp, S. Chi, J. Fernandez-Baca, M. Matsuda, D. A. Tennant, Y. Zhao, Z. Xu, J. W. Lynn, S. Huang, and M. Li, Topological singularity induced chiral Kohn anomaly in a Weyl semimetal, Phys. Rev. Lett. **124**, 236401 (2020).

[15] Z. Jin, B. Hu, Y. Liu, Y. Li, T. Zhang, K. Iida, K. Kamazawa, A. I. Kolesnikov, M. B. Stone, X. Zhang, H. Chen, Y. Wang, I. A. Zaliznyak, J. M. Tranquada, C. Fang, and Y. Li, Chern numbers of topological phonon band crossing determined with inelastic neutron scattering, Phys. Rev. B **106**, 224304 (2022).

[16] S. Shivam, R. Coldea, R. Moessner, and P. McClarty, Neutron scattering signatures of magnon Weyl points, arXiv:1712.08535.

[17] M. Elliot, P. A. McClarty, D. Prabhakaran, R. D. Johnson, H. C. Walker, P. Manuel, and R. Coldea, Order-by-disorder from bond-dependent exchange and intensity signature of nodal quasiparticles in a honeycomb cobaltate, Nat. Commun. **12**, 3936 (2021).

[18] A. Scheie, P. Laurell, P. A. McClarty, G. E. Granroth, M. B. Stone, R. Moessner, and S. E. Nagler, Dirac magnons, nodal lines, and nodal plane in elemental gadolinium, Phys. Rev. Lett. **128**, 097201 (2022).

[19] S. E. Nikitin, B. Fåk, K. W. Krämer, T. Fennell, B. Normand, A. M. Läuchli, and C. Rüegg, Thermal evolution of Dirac magnons in the honeycomb ferromagnet $CrBr_3$, Phys. Rev. Lett. **129**, 127201 (2022).

[20] See Supplemental Material at http://link.aps.org/supplemental/10.1103/PhysRevLett.131.246601, which contains Refs. [21–30], for the description of the methods, the analytical calculations of the IXS intensity winding, the details of fitting of the IXS momentum-energy maps, and the discussion of linearity of the phonon dispersion.

[21] M. Krisch and F. Sette, Inelastic x-ray scattering with very high resolution at the ESRF, Crystallogr. Rep. (Transl. Kristallografiya) **62**, 1 (2017).

[22] https://www.2dsemiconductors.com/.

[23] G. Kresse and D. Joubert, From ultrasoft pseudopotentials to the projector augmented-wave method, Phys. Rev. B **59**, 1758 (1999).

[24] G. Kresse and J. Furthmüller, Efficient iterative schemes for ab initio total-energy calculations using a plane-wave basis set, Phys. Rev. B **54**, 11169 (1996).

[25] G. Kresse and J. Furthmüller, Efficiency of ab initio total energy calculations for metals and semiconductors using a plane-wave basis set, Comput. Mater. Sci. **6**, 15 (1996).

[26] J. P. Perdew, K. Burke, and M. Ernzerhof, Generalized gradient approximation made simple, Phys. Rev. Lett. **77**, 3865 (1996).

[27] H. J. Monkhorst and J. D. Pack, Special points for Brillouin-zone integrations, Phys. Rev. B **13**, 5188 (1976).

[28] Y. Q. Cheng, L. L. Daemen, A. I. Kolesnikov, and A. J. Ramirez-Cuesta, Simulation of inelastic neutron scattering spectra using OCLIMAX, J. Chem. Theory Comput. **15**, 1974 (2019).

[29] A. Togo and I. Tanaka, First principles phonon calculations in materials science, Scr. Mater. **108**, 1 (2015).

[30] Y. X. Zhao and I. L. Spain, X-ray diffraction data for graphite to 20 GPa, Phys. Rev. B **40**, 993 (1989).

[31] J. Maultzsch, S. Reich, C. Thomsen, H. Requardt, and P. Ordejón, Phonon dispersion in graphite, Phys. Rev. Lett. **92**, 075501 (2004).

[32] M. Mohr, J. Maultzsch, E. Dobardžić, S. Reich, I. Milošević, M. Damnjanović, A. Bosak, M. Krisch, and C. Thomsen, Phonon dispersion of graphite by inelastic x-ray scattering, Phys. Rev. B **76**, 035439 (2007).

[33] A. Bosak, M. Krisch, M. Mohr, J. Maultzsch, and C. Thomsen, Elasticity of single-crystalline graphite: Inelastic x-ray scattering study, Phys. Rev. B **75**, 153408 (2007).

[34] A. Grüneis, J. Serrano, A. Bosak, M. Lazzeri, S. L. Molodtsov, L. Wirtz, C. Attaccalite, M. Krisch, A. Rubio, F. Mauri, and T. Pichler, Phonon surface mapping of graphite: Disentangling quasi-degenerate phonon dispersions, Phys. Rev. B **80**, 085423 (2009).

[35] K. H. Michel and B. Verberck, Theory of the evolution of phonon spectra and elastic constants from graphene to graphite, Phys. Rev. B **78**, 085424 (2008).

[36] J. Li, L. Wang, J. Liu, R. Li, Z. Zhang, and X.-Q. Chen, Topological phonons in graphene, Phys. Rev. B **101**, 081403(R) (2020).

[37] J. Li, J. Liu, S. A. Baronett, M. Liu, L. Wang, R. Li, Y. Chen, D. Li, Q. Zhu, and X.-Q. Chen, Computation and data driven discovery of topological phononic materials, Nat. Commun. **12**, 1204 (2021).

[38] B. Yuan, I. Khait, G.-J. Shu, F. C. Chou, M. B. Stone, J. P. Clancy, A. Paramekanti, and Y.-J. Kim, Dirac magnons in a honeycomb lattice quantum $CoTiO_3$, Phys. Rev. X **10**, 011062 (2020).

[39] A. Vishwanath and T. Senthil, Physics of three-dimensional bosonic topological insulators: Surface-deconfined criticality and quantized magnetoelectric effect, Phys. Rev. X **3**, 011016 (2013).

[40] L.-C. Zhang, Y. A. Onykiienko, P. M. Buhl, Y. V. Tymoshenko, P. Cermak, A. Schneidewind, J. R. Stewart, A. Henschel, M. Schmidt, S. Blugel, D. S. Inosov, and Y. Mokrousov, Magnonic Weyl states in Cu_2OSeO_3, Phys. Rev. Res. **2**, 013063 (2020).

[41] L. Chen, J.-H. Chung, B. Gao, T. Chen, M. B. Stone, A. I. Kolesnikov, Q. Huang, and P. Dai, Topological spin excitations in honeycomb ferromagnet CrI_3, Phys. Rev. X **8**, 041028 (2018).

[42] D. Xiao, M.-C. Chang, and Q. Niu, Berry phase effects on electronic properties, Rev. Mod. Phys. **82**, 1959 (2010).